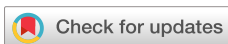


RESEARCH ARTICLE | JANUARY 29 2024

Broadband dual-comb hyperspectral imaging and adaptable spectroscopy with programmable frequency combs ^F

Special Collection: [State-of-the-Art and Future Directions in Optical Frequency Comb Sources, Enabling Technologies, and Applications](#)

Fabrizio R. Giorgetta ^{ORCID}; Jean-Daniel Deschênes ^{ORCID}; Richard L. Lieber ^{ORCID}; Ian Coddington; Nathan R. Newbury; Esther Baumann ^{ORCID} [✉]



APL Photonics 9, 010805 (2024)

<https://doi.org/10.1063/5.0179270>



CrossMark

AIP Photonics
 Special Topic: Brillouin Scattering and Optomechanics
 Submit Today

Broadband dual-comb hyperspectral imaging and adaptable spectroscopy with programmable frequency combs

Cite as: APL Photon. 9, 010805 (2024); doi: 10.1063/5.0179270
Submitted: 30 September 2023 • Accepted: 28 December 2023 •
Published Online: 29 January 2024



Fabrizio R. Giorgetta,^{1,2}  Jean-Daniel Deschênes,³  Richard L. Lieber,^{4,5}  Ian Coddington,¹
Nathan R. Newbury,¹ and Esther Baumann^{1,2,a)} 

AFFILIATIONS

¹National Institute of Standards and Technology, Communications Technology Laboratory, Boulder, Colorado 80305, USA

²Department of Physics, University of Colorado, Boulder, Colorado 80309, USA

³Octosig Consulting, Québec City, Québec G2K1X6, Canada

⁴Shirley Ryan Ability Lab Chicago, Chicago, Illinois 60611, USA

⁵Hines VA Medical Center Chicago, Chicago, Illinois 60141, USA

Note: This paper is part of the APL Photonics Special Topic on State-of-the-Art and Future Directions in Optical Frequency Comb Sources, Enabling Technologies, and Applications.

^{a)}Author to whom correspondence should be addressed: baumann@nist.gov

ABSTRACT

We explore the advantages of a free-form dual-comb spectroscopy (DCS) platform based on time-programmable frequency combs for real-time, penalty-free apodized scanning. In traditional DCS, the fundamental spectral point spacing, which equals the comb repetition rate, can be excessively fine for many applications. While fine point spacing is not itself problematic, it comes with the penalty of excess acquisition time. Post-processing apodization (windowing) can be applied to tailor the resolution to the sample, but only with a deadtime penalty proportional to the degree of apodization. The excess acquisition time remains. With free-form DCS, this deadtime is avoided by programming a real-time apodization pattern that dynamically reverses the pulse periods between the dual frequency combs. In this way, one can tailor the spectrometer's resolution and update rate to different applications without penalty. We show the operation of a free-form DCS system where the spectral resolution is varied from the intrinsic fine 160 MHz up to 822 GHz by applying tailored real-time apodization. Because there is no deadtime penalty, the spectral signal-to-noise ratio increases linearly with resolution by 5000× over this range, as opposed to the square root increase observed for post-processing apodization in traditional DCS. We explore the flexibility to change resolution and update rate to perform hyperspectral imaging at slow camera frame rates, where the penalty-free apodization allows for optimal use of each frame. We obtain dual-comb hyperspectral movies at a 20 Hz spectrum update rate with broad optical spectral coverage of over 10 THz.

© 2024 Author(s). All article content, except where otherwise noted, is licensed under a Creative Commons Attribution (CC BY) license (<http://creativecommons.org/licenses/by/4.0/>). <https://doi.org/10.1063/5.0179270>

I. INTRODUCTION

Dual-comb spectroscopy (DCS) probes many spectral signatures simultaneously with the broad spectrum of an optical frequency comb. Resolved spectra are generated by interference with a second comb and without a mechanical interferometer or dispersive elements. With fast update rates, no moving parts, and a coherent light source, DCS has often been promoted as a novel alternative to the classical Fourier transform infrared spectrometer (FTIR)

workhorse. Dual-comb spectrometers, however, still do not come with the versatility of FTIRs, particularly when it comes to adapting the spectral resolution and update rate to match the sample. Over the years, DCS has been applied to multiple spectroscopic applications, including high-precision molecular spectroscopy, open path green-house gas monitoring, breath analysis, fast molecular reaction measurements, and nonlinear spectroscopy.¹⁻³ What has not changed is the traditional operation scheme: two combs with rigidly fixed repetition rates, $\sim f_{rep}$, are used to interrogate the sample.

A preset repetition rate of the two underlying combs dictates the spectral point spacing, f_{rep} , and update rate of the instrument. Unfortunately, when a fine spectral point spacing is not needed, it restricts the achievable signal-to-noise ratio (SNR) by imposing an overly slow update rate. Thus, there is a need to introduce flexibility into the DCS probing paradigm. There are approaches that offer some f_{rep} tuning, such as electro-optic combs⁴ or optical cavity tuning.^{5–7} Here, we focus on modelocked lasers, which offer both broad spectral coverage and, in conjunction with our free-form DCS platform, dynamic and fast f_{rep} tuning.

The solution to optimizing resolution is real-time apodization, which was first proposed and implemented for DCS by translating an intracavity mirror using analog electronics in 2005,⁸ although the translation was not well controlled, making coherent averaging of signals difficult. In real-time apodization, the pulse period difference of the two comb sources is actively inverted repeatedly to record only a fraction of an interferogram with minimal dead time. This results in a loss in spectral resolution but a corresponding gain in update rate and SNR. This resembles electronically controlled optical sampling, where the repetition rate of one comb is steered with respect to the second comb.^{9–14} Here, we lock both a comb tooth to a narrow linewidth cw laser and the carrier envelope offset frequency (f_{ceo}), providing a 192 THz lever between the two lock points and superior phase coherence and timing precision of a few tens of attosecond.¹⁵ DCS with real-time apodization also operates in close analogy to an FTIR, where the physical scan can also be apodized in real-time,^{16,17} although the virtual scan possible with DCS does allow for faster scan speeds. One can also mimic apodized operation in traditional DCS in post-processing. However, such post-apodization only trades spectral resolution for deadtime; the fundamental spectrum update rate is unaltered, and SNR improvements are more modest.

Because of the challenges of controlling the frequency combs, DCS real-time apodization has not been further pursued until recently. Fortunately, recent advances in digital phase locking allow one to precisely program real-time apodization by digitally modulating the set points of the phase locks stabilizing the optical frequency comb.¹⁸ Here, we demonstrate real-time apodization with a single free-form dual-comb platform, which allows one to arbitrarily set the pulse time offsets between the combs with high precision.^{15,19} While real-time apodization has been used to increase measurement update rates,^{8,18} here we use free-form DCS to maintain coherent, attosecond control over the combs during the apodization, and we study the relation between spectral resolution, SNR, covered spectral bandwidth, and update rate.

We implement the free-form DCS using a robust, programmable, Er-fiber dual-comb platform with repetition rates of $f_{rep} = 160$ MHz. These low repetition rates offer ease of spectral tuning and spectral broadening through nonlinear processes due to higher pulse energies, along with fine intrinsic spectral point spacing and resolution. The finer spectral point spacing also captures narrow spectral features, such as \sim GHz wide atmospheric gas imprints, which could “slip” between comb teeth and go undetected for higher- f_{rep} DCS systems. By using real-time apodization, the resolution can be matched to the experimental requirements and is varied from 160 MHz to 822 GHz with no dead-time penalty, thus fully replicating the SNR of a DCS constructed with combs at equivalent repetition rates.²⁰

We also show that by decoupling the spectral resolution from the comb repetition rate, we can adapt the measurement rate to slow detectors, such as a camera focal plane array (FPA). Hyperspectral DCS imaging has recently been performed with electro-optic combs,^{21–25} but with free-form DCS and real-time apodization, it is now possible to harness the far broader spectral coverage possible with mode-locked lasers. Compared to single element photodetectors, infrared focal plane array cameras have slow update rates of at most a few kHz. Real-time apodization allows sufficient hyperspectral movie update rates to capture dynamic processes while covering unprecedented optical bandwidths. Here, we show a 20 Hz hyperspectral movie update rate while interrogating a >10 THz optical bandwidth, exceeding previous dual-comb hyperspectral imaging bandwidths by orders of magnitude.

II. REAL-TIME APODIZATION ON A FREE-FORM DCS PLATFORM

In DCS, the acquired interferogram is the product of the electric fields of two optical frequency combs at an array of relative pulse delays τ_{RPD} . Figure 1(a) shows an example of an interferogram as a function of τ_{RPD} . The interferogram depicts the time domain response of methane convolved with the time domain signal of the comb spectrum centered at 184 THz. The center part of the interferogram, around $\tau_{RPD} = 0$, is called a centerburst and contains information about the comb’s spectral envelope and any broad spectral signature of the sample. The tail of the interferogram contains the free induction decay signature corresponding to the narrow molecular features of methane. In traditional DCS, this interferogram is sampled monotonically, covering relative pulse delays ranging from $-1/(2f_{rep})$ to $1/(2f_{rep})$, as indicated by the gray dashed line in Fig. 1(b), yielding spectra at the intrinsic spectral point spacing of f_{rep} . When the acquired spectrum only contains features significantly broader than f_{rep} , there is no detectable signal toward the wings of the interferogram, and only noise is acquired at large $|\tau_{RPD}|$. In contrast, in real-time apodization, only a reduced portion, $|\tau_{RPD}| \leq \tau_{apod}/2$, of the interferogram is sampled, as indicated by the yellow arrow in Fig. 1(b).

If the resolution $f_{res} = 1/\tau_{apod}$ is matched to the sample’s spectral feature width, real-time apodization improves the SNR without loss of spectral information,²⁰ and the spectral SNR increases $\propto f_{res}/f_{rep}$. The measurement acquisition time per spectrum is $a\tau_{apod}$, where $a = \Delta f_r/f_{rep}$ is the programmable slew rate of the free-form dual-comb platform and denotes how fast τ_{RPD} changes per second, and Δf_r is the instantaneous difference between the two comb repetition rates. This same apodization can be carried out in post-processing by applying a window, as indicated by the solid green arrow in Fig. 1(b), but at the cost of a fractional deadtime of $1 - f_{rep}/f_{res}$ with the spectral SNR only increasing $\propto \sqrt{f_{res}/f_{rep}}$.

Note that frequency combs sample at discrete optical frequencies, and there is always a possibility of narrow spectral features slipping between the comb teeth. Apodization of a DCS spectrum will change the resolution without altering the comb teeth’s intrinsic frequencies, leading to potential confusion about the meaning of the word resolution. Here, we define resolution f_{res} as the inverse of the maximum pulse delay of the apodized interferogram as above, although it is important to keep the intrinsic frequency spacing in

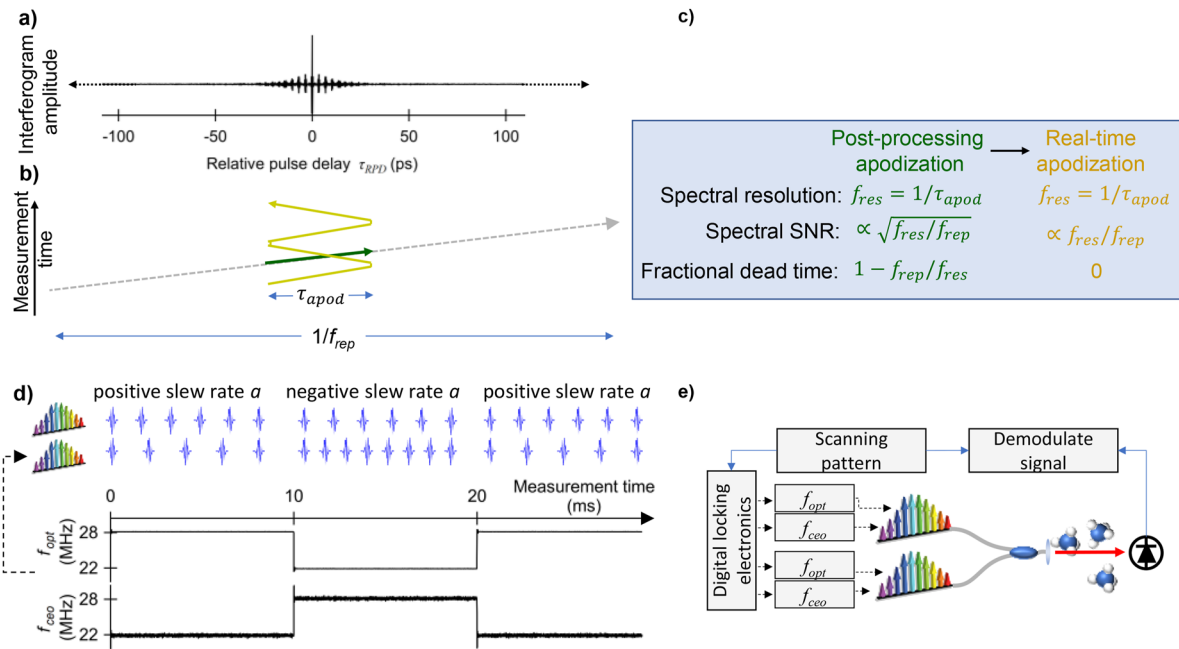


FIG. 1. Real-time apodization DCS overview. (a) Optical interferogram centerburst showing methane free-induction decay as a function of relative pulse delay. (b) Pulse delay scanning pattern. Gray dashed line: traditional DCS with fixed comb repetition rate. Green solid line: post-processing apodization, where only the centerburst is analyzed but the scan covers the same range as traditional DCS. Yellow line: real-time apodization. (c) Comparison of post-processing apodization to real-time apodization. (d) Schematic on how forward and backward triangular scanning is implemented in real-time apodization by modulating the rf lock frequencies f_{ceo} and f_{opt} to obtain a positive or negative slew rate, a . (e) Schematic of a free-form DCS setup. Here, only one comb is actively steered, but the setup is capable of steering both combs synchronously.

mind when sampling narrow spectral features. One advantage of the real-time apodization approach is that it can offer the improved SNR of a higher repetition rate comb while still capturing narrower spectral features.

Figures 1(d) and 1(e) show our measurement schematic and setup. We implement real-time apodized scanning on the phase stabilized free-form dual-comb platform¹⁹ using two Er-fiber mode locked lasers with $f_{rep} = 160$ MHz. The combs are phase stabilized by locking each f_{ceo} signal and by locking one comb tooth with f_{opt} to a common narrow linewidth single mode cw laser at frequency $\nu_{cw} \approx 191.56$ THz, with $f_{ceo} = f_{opt} = 25$ MHz. To implement the continuous triangular τ_{RPD} scanning pattern for a given τ_{apod} , a corresponding dynamic phase profile is calculated in a digital signal processor and applied to the locking frequencies f_{ceo} and f_{opt} of the digital locking electronics. This effectively shifts f_{ceo} and f_{opt} and causes the dual-comb pulses to lead or lag, resulting in a positive or negative slew rate, a (see also the Appendix).

Here, we apply real-time apodization to mode-locked lasers, which are mature and can easily be broadened to cover wide spectral regions. In addition, mode-locked lasers with lower repetition rates have the most to gain from real-time apodization to avoid oversampling. One could also use different dual-comb platforms as long as they are tightly controlled, such as electro-optic combs, and as long as the interferogram remains relatively compressed (i.e., the differential chirp between both combs has to be low).

III. TAILOR SPECTRAL RESOLUTION AND UPDATE RATE WITH REAL-TIME APODIZATION

Here, we experimentally analyze the SNR and update rate for different real-time apodization scans by measuring narrow methane and broad isoprene absorption features. Figure 2(a) shows the measurement setup. The combs are spectrally broadened and filtered to cover >10 THz, encompassing the Q and R branches of the methane ¹²CH₄, 2ν₃ (0020 F2) transitions, as well as the broad isoprene overtone absorption feature around 184 THz. The combined comb light is collimated and sequentially probes a 75 cm long cell filled with 40% methane in air at 60 hPa and a 6 cm long cell filled with 100% isoprene at 1100 hPa. The dual-comb spectrum through each of these cells is shown on the right panel in Fig. 2(a) independently.

Figure 2(b) shows real-time apodized interferograms for relative pulse delay windows, τ_{apod} , ranging from the maximum $1/f_{rep} = 6.25$ ns down to consecutively shorter apodization windows of 389 and 22 ps, correspondingly degrading the spectral resolution from 160 MHz to 2.57 GHz and 45 GHz. At a DCS slew rate of $a = 33$ ns/s, the measurement time per spectrum drops from $T_{apod} = 192$ ms to 12 ms and 0.749 ms (taking into account some scan turnaround time; see the Appendix). This slew rate is limited by the dynamic range and speed of the comb actuators, in our case an intracavity piezoelectric transducer, and the current modulation of a pump laser diode (see the Appendix).

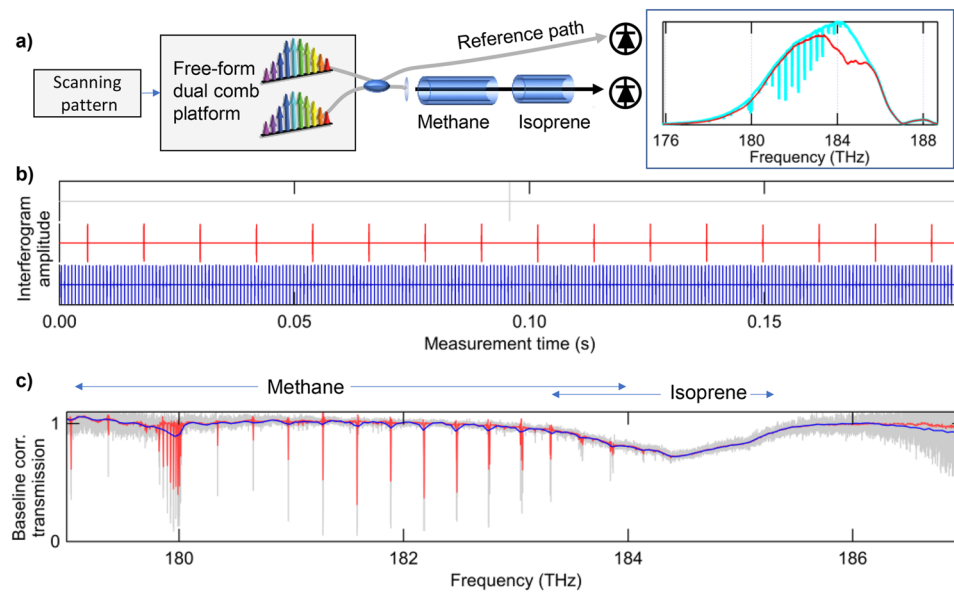


FIG. 2. Experimental real-time apodization. (a) Setup. A triangular scanning pattern sets the maximum relative pulse delay, or apodization window, between the two combs. The combined light probes methane and isoprene in cells, as well as a reference path. The measured DCS spectrum is shown on the right for just methane (blue) and just isoprene (red). (b) Measured real-time apodized interferogram for $T_{\text{apod}} = 192$ ms (top), 12 ms (middle), and $749 \mu\text{s}$ (bottom). Centerbursts appear as vertical lines at this scale. The shorter the T_{apod} , the more interferograms are measured, improving the SNR at the cost of spectral resolution. (c) Corresponding transmission spectra, normalized with the reference path spectra, showing methane and isoprene features. Each is averaged over 766 ms. As the real-time apodization window shrinks, one observes the expected increase in SNR and loss of spectral resolution, particularly evident for the ~ 1 GHz wide methane features.

Figure 2(c) shows the corresponding normalized transmission spectra, averaged over 766 ms. Methane shows many distinct narrow spectral absorption features, and isoprene, a heavier molecular compound, has a broad overall structure lacking narrow features at atmospheric pressure. The broadband isoprene feature is observed at full fidelity for all resolutions, whereas the ~ 1 GHz wide methane lines are broadened and become less distinct at coarser spectral resolutions. This is because, as mentioned above, akin to FTIR, apodization introduces an instrument line shape for spectral resolutions larger than the spectral feature width. This spectral line shape is the Fourier transform of the effective square-top apodization window in the time domain.

For the $a = 33$ ns/s slew rate used here, a single, unapodized measurement at the full 160-MHz spectral point spacing and resolution takes 192 ms. Figure 3(a) shows a real-time apodization measurement taken at a much shorter 12-ms acquisition time with a corresponding resolution of $f_{\text{res}} = 2.57$ GHz. This spectrum is fit to a model consisting of methane and isoprene and a cubic polynomial baseline. The isoprene model is taken from the PNNL database.²⁶ The methane model is calculated at fine spectral point spacing (here, we use 160 MHz) using Voigt lineshapes and HITRAN 2008²⁷ line shape parameters and converted to 2.57 GHz resolution by calculating its inverse Fourier transform, applying the 389 ps apodization window, and finally Fourier transforming back into the spectral domain (see the Appendix for a detailed description of the analysis). As shown in Fig. 3(b), 128 such measurements were acquired over 1.53 s. We can contrast this to traditional DCS followed by post-processing apodization to achieve the same $f_{\text{res}} = 2.57$ GHz.

In that case, the acquisition time is fixed at 192 ms, and only eight measurements are acquired over 1.53 s.

Figures 3(c)–3(e) compare real-time apodized DCS to traditional DCS for varying apodization window widths and, thus, resolutions. Figure 3(c) shows the spectral SNR (see the Appendix for SNR calculation) as a function of spectral resolution f_{res} . For real-time apodized measurements, a linear increase in SNR is observed, which is the same dependence as for varying the fundamental repetition rate f_{rep} of the DCS system.²⁰ This represents a significant improvement over the $\propto \sqrt{f_{\text{res}}/f_{\text{rep}}}$ SNR scaling achieved by smoothing a traditional DCS spectrum through post-processing apodization.

The standard error on the extracted gas number densities as a function of resolution is shown in Figs. 3(d) and 3(e) for a 1.53 s acquisition time. For isoprene, a large compound molecule with broad spectral features [see Fig. 2(a)], it improves $\propto \sqrt{f_{\text{res}}/f_{\text{rep}}}$ for the real-time apodized data due to the increasing number of measurements within the same time, while it remains flat for traditional DCS. Note that, as expected, post-processing apodization, a form of smoothing, improves the spectral SNR [Fig. 3(c)] but not the number density standard error. For methane, the narrow feature linewidth complicates this simple trend. The standard error first decreases with coarser resolution up to the ~ 1 GHz width of the methane features and then plateaus. We attribute this to the increased crosstalk between the apodized methane model and the cubic baseline.

These data demonstrate the advantages of a flexible DCS system with real-time apodization. A coarser resolution can be

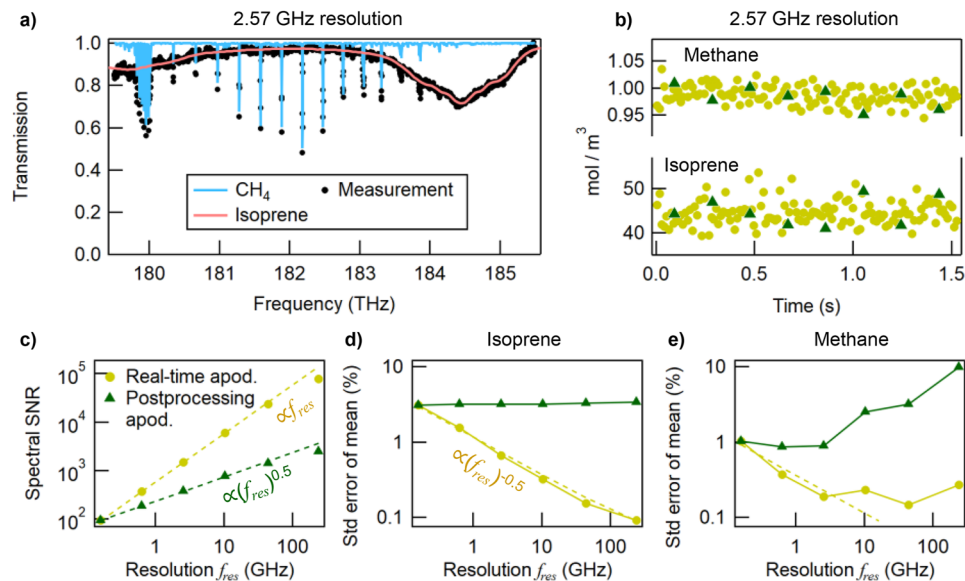


FIG. 3. Spectral analysis. (a) Normalized transmission spectrum and fit for a single 2.57 GHz resolution measurement showing the measured spectrum after correction with a cubic polynomial baseline and the fitted methane and isoprene spectra. (b) Fitted number density for methane (75 cm long cell) and isoprene (6 cm long cell) at $f_{res} = 2.57$ GHz acquired over 1.53 s. Yellow circles denote real-time apodization; green triangles denote post-processing apodization. (c) Spectral SNR for real-time vs post-processing apodization for different spectral resolutions and a fixed 1.53 s acquisition time. (d) Standard error of the mean for the isoprene number density. (e) Standard error of the mean for the methane number density.

chosen to increase the update rate and, hence, the SNR within a given measurement time. On the other hand, one can run the same DCS at fine resolution to measure narrow absorbers with high fidelity, e.g., for decluttering of multiple species or line shape characterization.

IV. REAL-TIME APODIZATION FOR HYPERSPECTRAL IMAGING

Hyperspectral imaging, where one seeks information about the spatial distribution of spectral content in a scene or a sample, is applied to chemical and remote earth sensing, quality control, and medical science.^{28–31} Dual-comb spectroscopy, with its broad spectral coverage, $\Delta\nu$, and direct mapping of the optical signal into the RF domain, is promising for hyperspectral imaging of gases, for example. One limitation is that cameras in the near and mid-infrared, where most gases have strong spectral features, have slow frame rates, R . Matching the RF bandwidth of the optical broad-band DCS signal to this low framerate is challenging, especially for sub-GHz repetition rate combs. For traditional DCS, the maximum hyperspectral movie update rate is given by $R_{hyp} = \Delta f_r \leq f_{rep}R/(2\Delta\nu)$. For a $\Delta\nu = 20$ THz wide optical signal, a $R = 1$ kHz camera framerate, and a $f_{rep} = 160$ MHz DCS system, the maximum hyperspectral frame rate is 0.002 Hz, or one image every 500 s. Researchers have circumvented this issue by using high repetition-rate EO-combs and have demonstrated hyperspectral update rates of 0.5–10 Hz at sub-THz spectral bandwidth.^{21–25}

Here, we take advantage of the versatility of real-time apodization to trade spectral resolution, update rate, and optical bandwidth.

The triangular apodized τ_{RPD} scanning pattern is defined by two parameters: the measurement time per scan, T_{apod} , and the slew rate a . For a desired update rate R_{hyp} and optical bandwidth $\Delta\nu$, one then sets $a = R/(2\Delta\nu)$ and $T_{apod} = 1/R_{hyp}$, resulting in an optical resolution of $f_{res} = 1/(aT_{apod})$. This interdependence is shown in Fig. 4(a). Again, this is analogous to using a higher-repetition rate dual-comb spectrometer with $f_{rep} = f_{res}$. As shown in Fig. 4(a), real-time apodization can support both broad spectral coverage and fast hyperspectral update rates independent of frequency comb repetition rate, other than $f_{res} \geq f_{rep}$.

As a demonstration, we select the hyperspectral imaging conditions indicated by the blue solid lines in Fig. 4(a), namely a hyperspectral movie update rate of $R_{hyp} = 20$ Hz and a spectral coverage of $\Delta\nu = 20.6$ THz, resulting in a spectral resolution of $f_{res} = 822$ GHz, suitable for a larger molecular compound. The spectral coverage exceeds previous hyperspectral dual-comb demonstrations by orders of magnitude.^{21–25}

Figure 5(a) shows individual frames of a movie acquired over a few seconds that record liquid isoprene drops falling into a glass cell and then evaporating [see Fig. 4(b) for measurement setup]. The raw camera output generates 12-bit monochrome intensity images of the cell illuminated by the dual-comb light. The images are then grouped in sequences of 50, corresponding to a single apodized scan. Each sequence is then Fourier transformed for each pixel, yielding a hyperspectral movie at a $R_{hyp} = 20$ Hz update rate. Figure 5(b) shows raw spectra for a single pixel at different times, where the developing isoprene signature is clearly visible around 184 THz. The spectra of each pixel are first normalized by an empty-cell background spectrum and a third-order polynomial baseline. They are then fitted to

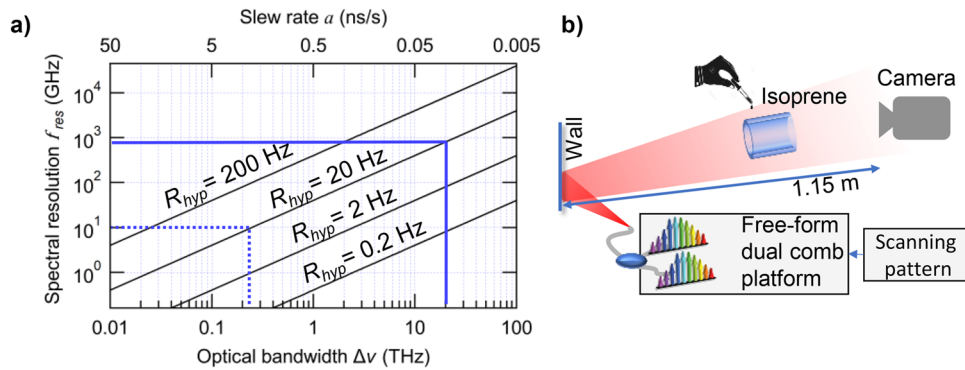


FIG. 4. Hyperspectral imaging. (a) Relationship between spectral resolution and maximum optical bandwidth coverage for real-time apodization at a 1 kHz camera frame rate. The diagonal lines correspond to the labeled hyperspectral movie frame rates. In our example, highlighted by the blue lines, a 20 Hz hyperspectral movie update rate is achieved with 20 THz spectral coverage and 822 GHz spectral resolution. Another example, highlighted by blue dashed lines, might be appropriate for narrower absorbers with a spectral resolution of 10 GHz and an optical bandwidth of 250 GHz. (b) Hyperspectral imaging setup. The combs are combined in fiber and sent into free space from a fiber connector tip. Their diverging light (~ 3 mW) diffusely illuminates an open cell, which is filled with liquid isoprene that then evaporates. An InGaAs camera captures the scene.

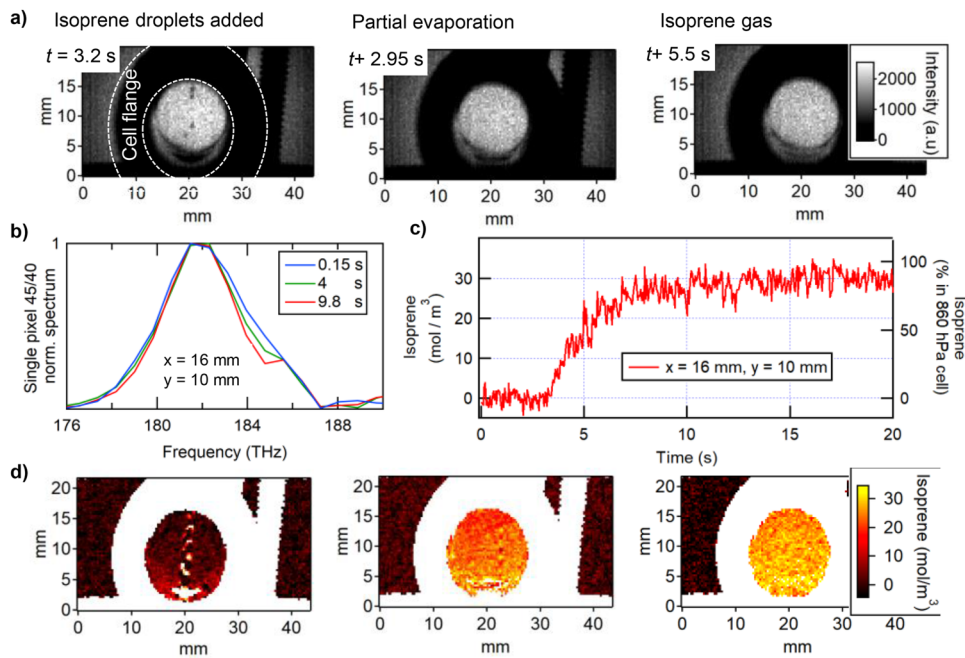


FIG. 5. Hyperspectral imaging with a 128×64 pixel InGaAs NIR camera of isoprene evaporating in a 15 mm wide and 80 mm long cell. (a) Raw images from the 1 kHz frame rate movie. Isoprene droplets are added 3.2 s into the measurement and then evaporate over the next few seconds. In the intensity images, the isoprene gas is not visible. (b) Example DCS spectra of a single pixel inside the cell at the selected 822 GHz spectral resolution. The time-varying isoprene signature is clearly visible around 184 THz. (c) Time evolution of the extracted isoprene gas concentration for the same single pixel over the entire movie duration. (d) Example isoprene concentration images at times indicated in (a). The acquisition rate is $R_{hyp} = 20$ Hz. Note that the isoprene droplets are not stationary at this frame rate and cause distortion in the measured spectra of these pixels, resulting in nonsensical extracted isoprene concentrations around the falling droplets at 3.2 s. See the supplementary material for the full isoprene concentration movie.

an isoprene model,²⁶ yielding isoprene gas time evolution as shown for a single pixel in Fig. 5(c). After 10 s, the isoprene concentration is 28 mol/m^3 , the equivalent of 82% isoprene at atmospheric conditions in the cell. Figure 5(d) shows example isoprene concentration images at different times.

V. CONCLUSIONS

Real-time apodization expands the measurement capabilities of a dual-comb platform for spectroscopic sensing. It can diversify the applications of a single DCS platform to optimally detect atmospheric trace gases, large molecules, liquids, and solids, for

example, in photo-acoustic measurements^{32,33} or muscle tissue measurements where broad spectral coverage and a fast update rate are needed while coarse spectral resolution is adequate.³⁴ We show that a free-form dual-comb spectrometer using programmable combs can break free from the traditional preset and fixed repetition rates of the combs used in traditional DCS.

We demonstrate and analyze spectral resolution tuning ranging from 160 MHz to 822 GHz by only acquiring a fraction of the optical interferogram in real time. The spectral SNR increases linearly with the resolution, such as when using a higher repetition rate comb source, but this system retains the advantage of a sub-GHz comb source's high-power pulses for spectral broadening and tuning and narrow spectral comb tooth spacing. The programmable real-time apodization enables direct comb hyperspectral imaging at over 10 THz optical bandwidth, orders of magnitude broader than previous demonstrations using high repetition rate frequency combs.

SUPPLEMENTARY MATERIAL

Spatially resolved movie (x/y) of varying isoprene concentrations extracted from hyperspectral dual-comb spectroscopic cubes (spatial x/y and optical frequency). See also Fig. 5(d) for three individual frames.

ACKNOWLEDGMENTS

We thank T. Bui and B. Washburn for their technical comments and acknowledge funding from the Rehabilitation Institute of Chicago (Shirley Ryan AbilityLab) subaward No. 80335 UCB.Y1 and NIST.

AUTHOR DECLARATIONS

Conflict of Interest

The authors have no conflicts to disclose.

Author Contributions

Fabrizio R. Giorgetta: Conceptualization (equal); Data curation (equal); Formal analysis (equal); Investigation (equal); Methodology (equal); Resources (equal); Software (equal); Validation (equal); Visualization (equal); Writing – original draft (equal); Writing – review & editing (equal). **Jean-Daniel Deschênes:** Conceptualization (equal); Software (equal). **Richard L. Lieber:** Funding acquisition (equal); Writing – review & editing (supporting). **Ian Coddington:** Conceptualization (equal); Funding acquisition (supporting); Writing – review & editing (equal). **Nathan R. Newbury:** Conceptualization (equal); Funding acquisition (supporting); Writing – review & editing (equal). **Esther Baumann:** Conceptualization (equal); Data curation (equal); Formal analysis (equal); Funding acquisition (lead); Investigation (equal); Methodology (equal); Project administration (equal); Resources (equal); Software (equal); Supervision (equal); Validation (equal); Visualization (equal); Writing – original draft (equal); Writing – review & editing (equal).

DATA AVAILABILITY

The data that support the findings of this study are available from the corresponding author upon reasonable request.

APPENDIX: PHASE LOCK ADJUSTMENT IN FREE-FROM DUAL-COMB SPECTROSCOPY

Figure 6 schematically depicts how the triangular forward and backward scanning over the optical interferogram is implemented. The upper row is a cartoon of how, first, the relative pulse offset is increasing and the pink comb pulses walk over the blue comb pulses, and after changing the pulse periods, the relative pulse offset is decreasing and the blue pulses walk over the pink pulses (lower row).

The traditional dual-comb sampling is based on a preset difference $\Delta f_r = f_{r1} - f_{r2}$ with an acquisition time of $1/\Delta f_r$, and, assuming both combs probe the sample, a preset resolved spectral point spacing of $(f_{r1} + f_{r2})/2 \approx f_{rep}$, which means that the interferogram is always sampled from $-1/(2f_{rep})$ to $+1/(2f_{rep})$ with fixed increments in relative pulse offsets of $\Delta f/f_{rep}^2$. In order to break these preset relationships, we adapt the phase locking of the combs,^{15,19} see Fig. 6(b). While phase coherence can be established via different means, here, we lock two frequencies, f_{ceo} and ν_{opt} . The carrier-envelope-offset frequency $f_{ceo} = r_0 f_{rep}$ is stabilized via an $f-2f$ setup. N is the tooth number nearest to a cw reference laser at $\nu_{cw} = 191.56$ THz (6390 cm⁻¹), and $\nu_{opt} = \nu_{cw} - r_N f_{rep} = \nu_{cw} - f_{opt}(r_0$ and r_N , $r \in \mathbb{Q}$, $-1/2 < r < 1/2$). This approach gives fine control of $f_{rep} = (\nu_{opt} - f_{ceo})/N = \nu_{cw}/(N + r_0 + r_N)$ due to the large spacing in frequency between $f_{rep} \sim 160$ MHz and $\nu_{opt} \sim 191.56$ THz and $N \sim 1.2 \times 10^6$.

After setting both combs to the same repetition rate and establishing full dual-comb pulse overlap, the relative dual-comb pulse delay τ_{RPD} is changed by programming the control phases $\Delta\theta_0^1, \Delta\theta_0^2, \Delta\theta_N^1, \Delta\theta_N^2$ of the digital f_{ceo} and f_{opt} locks acting on both combs (superscript 1 and 2), resulting in a time shift,

$$\Delta\tau(t) = \frac{\Delta\theta_0^1(t) + \Delta\theta_0^2(t) - \Delta\theta_N^1(t) - \Delta\theta_N^2(t)}{2\pi N f_{rep}}. \quad (A1)$$

We only modulate comb 1 and use $\Delta\theta_0^1(t) = -\Delta\theta_N^1(t)$ $= \Delta\theta(t)$, resulting in

$$\Delta\tau(t) = \frac{\Delta\theta(t)}{\pi N f_{rep}}. \quad (A2)$$

The slew rate at which the relative pulse-offset is changing is $a = \Delta f_r(t)/f_{rep}$, and τ_{RPD} is swept between $-1/(2f_{res})$ and $+1/(2f_{res})$, where $f_{res} = 1/\tau_{apod} = 1/(aT_{apod})$ is the desired spectral resolution and T_{apod} is the acquisition time for one sweep.

Our two actuators have a maximum throw of 3.125 MHz on f_{ceo} (current modulation) and f_{opt} (a fast piezo-electric transducer), resulting in $\Delta f_r = (2 \times 3.125 \text{ MHz}/N) = 5.2$ Hz and a slew rate of 5.2 Hz/160 MHz = 33 ns/s. This slew rate is not a fundamental limit and could be doubled by steering all four locks synchronously.¹⁵ Other limiting factors specific to our setup are the actuator throw and the fixed digital bandpass filter center frequency of the digital locks.

When scaling the measured spectrum back to the optical domain, the change to the CEO lock frequency has to be considered, and comb teeth overlap is shifted from 0 to $\delta f_{ceo} f_{rep}/\Delta f_r$, where δf_{ceo} is the total amount of one or both shifts to the CEO lock frequency f_{ceo} .

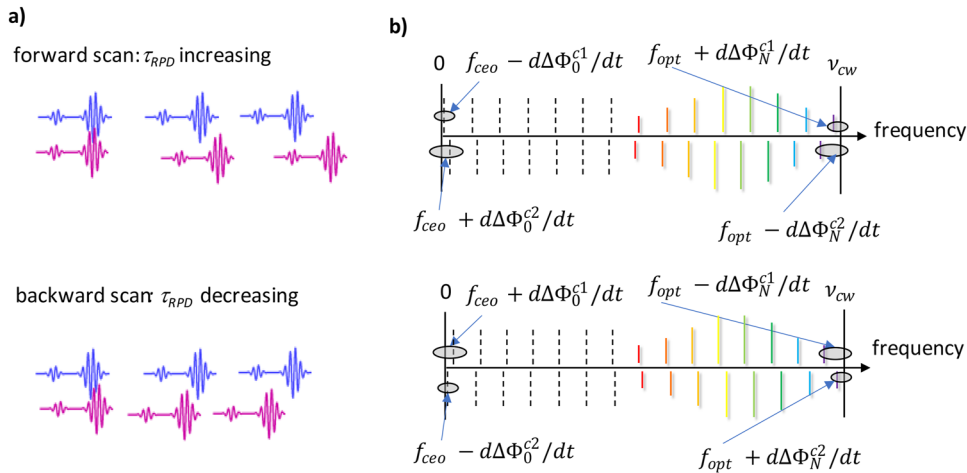


FIG. 6. Schematic overview of (a) time and (b) frequency domains for real-time apodized scanning. To initiate scanning of the dual-comb pulses' relative delays, the combs are first set to the same repetition rate, followed by phase offsets, with the appropriate signs to the phase locks.

There is a small deadtime in real-time apodization caused by the finite bandwidth of the frequency comb actuators. Here, the f_{CEO} lock frequency is modulated via the pump diode current at an amplitude of ± 3.125 MHz, and it takes about $50 \mu\text{s}$ for the f_{CEO} to settle after a comb pulse period reversal (see Fig. 7). For the apodized data presented in this manuscript, the first $50 \mu\text{s}$ of each sweep are not used and present effectively dead time. This could be improved by either using faster actuators or digitally correcting for the frequency transient immediately following jumps by calculating the effective pulse offset time of each interferogram point and resampling on an equidistant grid.⁸

1. Spectral SNR calculation and spectral sampling grid

Figure 8 describes how the spectral SNR shown in the main body Fig. 3(c) is calculated, assuming dominating white additive noise. For N coherently averaged measurements, we define the

signal as the peak magnitude value and the noise as the expected value (mean) in the absence of light in the corresponding magnitude spectrum, for the following reasons.

The N real-valued measured interferograms are Fourier transformed to obtain N complex-valued spectra with additive white noise. For the corresponding magnitude spectra, the noise of each spectrum follows a rice distribution, which becomes a Rayleigh distribution in the absence of light (and, thus, signal) with a mean μ_1 and a standard deviation $sdev_1$. If the N complex spectra are averaged and the magnitude is calculated from this averaged spectrum, the noise (in the absence of a signal) still follows a Rayleigh distribution, and its mean is proportional to the standard deviation, namely $\mu_N = \mu_1/\sqrt{N} = sdev_N\sqrt{\pi/(4-\pi)}$, where $sdev_N = sdev_1/\sqrt{N}$ [see Fig. 8(e)]. In addition, when the complex spectra are phase corrected prior to averaging,³⁵ the signal peak value remains unchanged throughout the averaging. The SNR increases with \sqrt{N} , regardless of whether the noise is estimated from the

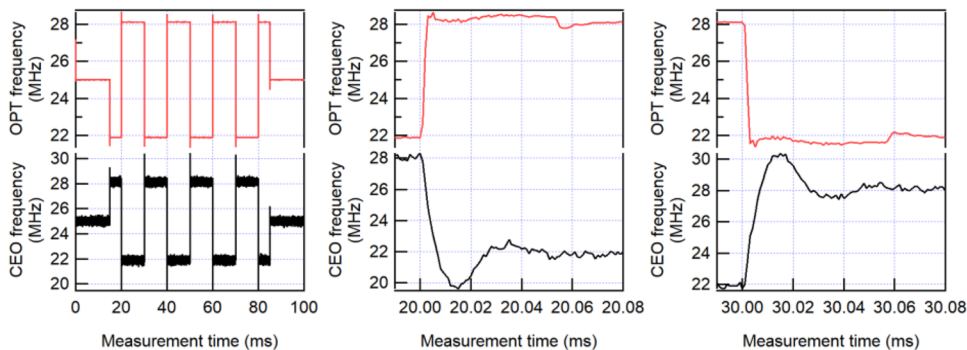


FIG. 7. Actuator response for CEO and optical (OPT) instantaneous lock frequency beat for a ± 3.125 MHz jump around the 25 MHz set value. The CEO lock, modulated via the oscillator pump diode current, has a slower response and takes about $50 \mu\text{s}$ to fully settle. The optical lock, modulated via a fast intracavity PZT, is faster and is mostly settled after $5 \mu\text{s}$. The response is antisymmetric in both directions.

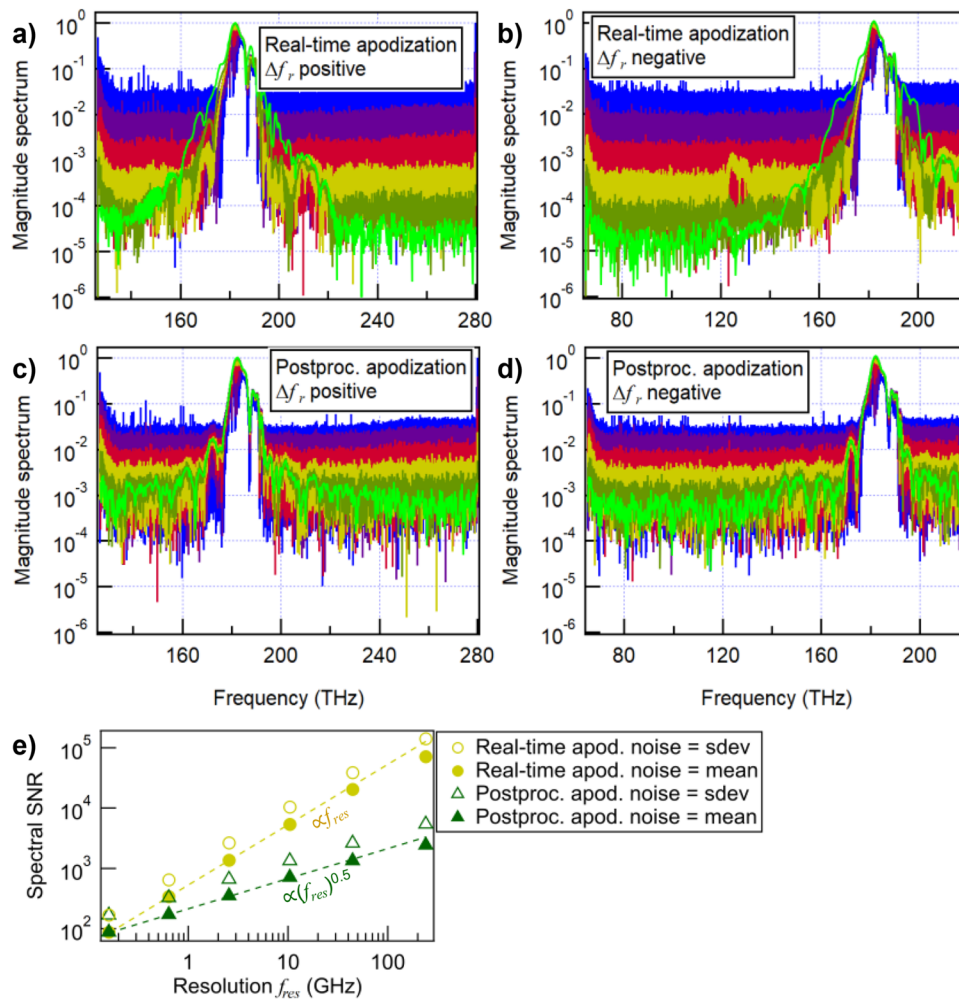


FIG. 8. (a–d) Acquired spectra averaged over a measurement time of 1.53 s for real-time apodization (top panels) and post-processing apodization of fully resolved spectra (bottom panels). Each trace corresponds to a specific resolution, ranging from 160 MHz (blue, highest noise level) to 241 GHz (bright green, lowest noise level). To obtain the averaged magnitude spectrum for a given resolution, the complex spectra are phase corrected, averaged, and transformed to magnitude. Because the pulse period of the combs changes between consecutive acquisitions, the optical span covered is different for ‘positive’ and ‘negative’ scan directions, as shown in the left vs right panels. The signal is defined as peak magnitude, and the noise is estimated from the magnitude spectrum between 250 and 260 THz for the positive scan direction, respectively, and between 100 and 110 THz for the negative scan direction. (e) Impact of using the standard deviation or the mean for noise level estimation on SNR numbers. Figure 3(c) in the main manuscript uses the mean.

standard deviation or the mean. Here, we choose to calculate the SNR with respect to the mean of the noise between 250 and 260 THz for the positive scan direction and, respectively, between 100 and 110 THz for the negative scan direction.

Note that if the magnitude spectra were calculated for each of the N spectra and the averaging was performed directly with these magnitude spectra, no phase alignment would be necessary to retain the signal peak value, but the noise in the averaged magnitude spectrum in the absence of a signal would approach a normal distribution (central limit theorem) with $\mu_N = \mu_1$ and $sdev_N = sdev_1/\sqrt{N}$. In this case, the SNR would scale with \sqrt{N} when estimating the noise with the standard deviation but remain constant when using the mean.

As shown in Fig. 8, the positive and negative apodized scans introduce different spectral mapping, which is due to the change in comb phase-lock frequencies that move the optical comb teeth frequencies. As a side effect, this introduces interleaving beyond the comb tooth spacing f_{rep} since the positive and negative scan directions probe the spectrum on an offset spectral grid.

2. Spectral fitting

This section describes in detail how isoprene and methane number densities are extracted from the raw measured spectra through an isoprene and methane cell. The experimental setup is shown in Fig. 2(a) of the main manuscript.

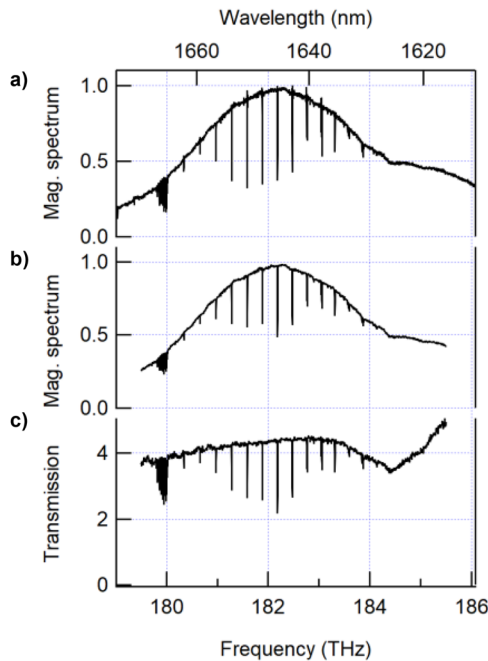


FIG. 9. Spectrum preparation prior to isoprene/methane fitting shown for 2.57 GHz resolution. (a) Raw spectrum apodized to 2.57 GHz showing the spectral signature of the DCS (overall baseline), methane (narrow lines), and isoprene (broad feature, most prominent around 184.5 THz). (b) Same spectrum spanning 179.5 to 185.5 THz after applying a Hann window. (c) Spectrum from (b) normalized with a reference spectrum acquired simultaneously on a separate acquisition channel [see Fig. 2(a)].

Only spectral data between 179.5 and 185.5 THz is used for fitting. After cropping the spectrum, the raw signal spectrum shown in Fig. 9(a) is then inverse Fourier transformed, multiplied with a Hann window, and Fourier transformed to obtain the windowed spectrum shown in Fig. 9(b). This is done to reduce the ringing surrounding the narrow methane features, which increases fit robustness. The windowed signal spectrum is then divided by a reference spectrum that was previously smoothed to a 20 GHz resolution to avoid adding excess noise; Fig. 9(c).

This normalized transmission spectrum is then fit with an iterative nonlinear least-squares Levenberg–Marquardt algorithm to the model,

$$(c_0 + c_1p + c_2p^2 + c_3p^3) \times \exp(-c_4 \times isop_{PNNL} - c_5 \times CH_{4Hitran}),$$

where p is the frequency bin index, c_x are the floating fit parameters: $c_0, c_1, c_2,$ and c_3 are the cubic polynomial baseline parameters; c_4 is the path integrated isoprene concentration at 1013.25 hPa and 296 K; and c_5 is the path integrated methane concentration at 60 hPa and 296 K. Finally, using the known gas cell lengths $l_{isocell} = 0.06$ m and $l_{CH_4cell} = 0.75$ m, c_4 and c_5 are converted to the number densities, ND , reported in the main body via the ideal gas law,

$$ND_{iso} = c_4/l_{isocell} \times \frac{101325}{296 \times R}, \quad ND_{CH_4} = c_5/l_{CH_4cell} \times \frac{6000}{296 \times R}$$

where $R = 8.31446261815324$ J/K/mol is the molar gas constant.

The isoprene spectrum of $isop_{PNNL}$ is taken from the PNNL database,²⁶ which provides a measured reference spectrum at 296 K and 101325 Pa. The methane spectrum of $CH_{4Hitran}$ is calculated using HITRAN 2008 with a Voigt line shape. First, both the methane concentration and the methane cell ambient pressure were

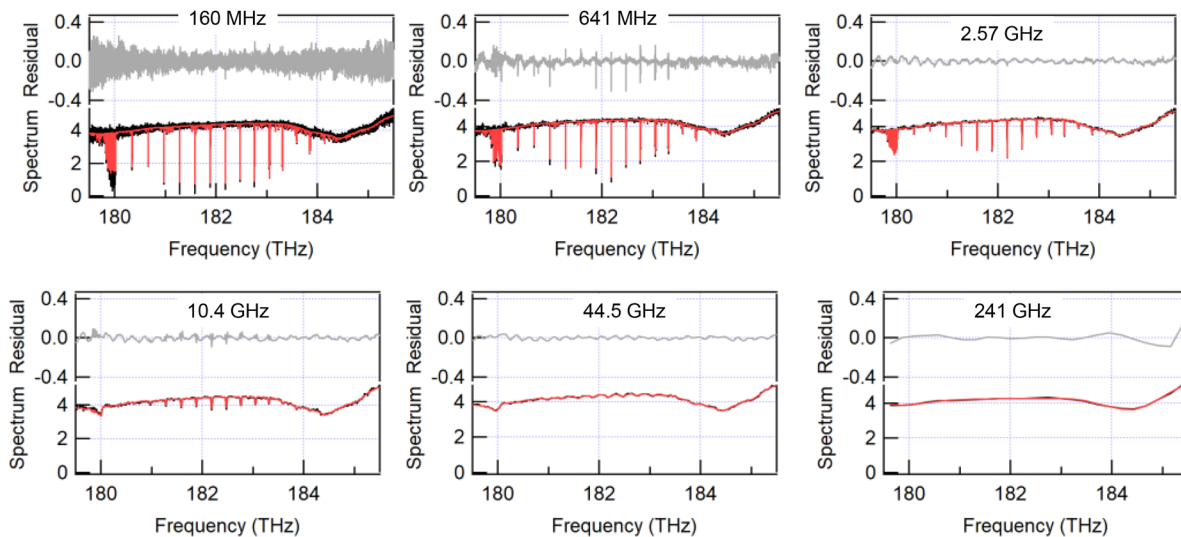


FIG. 10. Normalized transmission spectra of methane and isoprene are shown in black for the spectral resolution as labeled in the panels. Red: transmission model based on HITRAN 2008 (CH_4)²⁷ and PNNL (isoprene)²⁶ databases, using a Hann apodization window, for a single scan. Top (gray), residuals to the fit, averaged over the entire measurement time of 1.53 s to highlight structure not captured by the fit model.

fit with the 160 MHz resolution spectra, resulting in a fitted ambient methane gas cell pressure of 6000 Pa and a methane concentration of 40%. Then, the methane model $\text{CH}_4^{\text{Hitran}}$ was calculated for these conditions and scaled with a fit concentration coefficient of c_5 for all fits. Finally, both $i\text{SO}_{\text{PNNL}}$ and $\text{CH}_4^{\text{Hitran}}$ are apodized to the resolution of the measurement, and a Hann window is applied to the model.

Figure 10 gives an overview of the good fit qualities at all measured spectral resolutions when applying the adequate apodization window to the model. At $f_{\text{res}} = 241$ GHz, τ_{RPD} is scanned symmetrically from -2.07 ps to $+2.07$ ps. The first methane recurrence is not covered anymore, the spectral resolution is close to the periodic line spacing of the lines, and the fit result for methane is strongly influenced by baseline crosstalk. Isoprene, on the other hand, is still captured reliably.

REFERENCES

- I. Coddington, N. Newbury, and W. Swann, "Dual-comb spectroscopy," *Optica* **3**, 414–426 (2016).
- N. Picqué and T. W. Hänsch, "Frequency comb spectroscopy," *Nat. Photonics* **13**, 146–157 (2019).
- K. C. Cossel, E. M. Waxman, E. Baumann, F. R. Giorgetta, S. C. Coburn, C. B. Alden, and B. R. Washburn, "2-remote sensing using open-path dual-comb spectroscopy," in *Advances in Spectroscopic Monitoring of the Atmosphere*, edited by W. Chen, D. S. Venables, and M. W. Sigrist (Elsevier, 2021), pp. 27–93.
- V. Torres-Company and A. M. Weiner, "Optical frequency comb technology for ultra-broadband radio-frequency photonics: Optical frequency comb technology for RF photonics," *Laser Photonics Rev.* **8**, 368–393 (2014).
- T. Hochrein, R. Wilk, M. Mei, R. Holzwarth, N. Krumbholz, and M. Koch, "Optical sampling by laser cavity tuning," *Opt. Express* **18**, 1613 (2010).
- S. Potvin, S. Boudreau, J.-D. Deschênes, and J. Genest, "Fully referenced single-comb interferometry using optical sampling by laser-cavity tuning," *Appl. Opt.* **52**, 248–255 (2013).
- H. Wu, F. Zhang, T. Liu, P. Balling, J. Li, and X. Qu, "Long distance measurement using optical sampling by cavity tuning," *Opt. Lett.* **41**, 2366–2369 (2016).
- A. Schliesser, M. Brehm, F. Keilmann, and D. van der Weide, "Frequency-comb infrared spectrometer for rapid, remote chemical sensing," *Opt. Express* **13**, 9029–9038 (2005).
- F. Tauser, C. Rausch, J. H. Posthumus, and F. Lison, "Electronically controlled optical sampling using 100 MHz repetition rate fiber lasers," in *Commercial and Biomedical Applications of Ultrafast Lasers VIII* (SPIE, 2008), pp. 139–146.
- Y. Kim and D.-S. Yee, "High-speed terahertz time-domain spectroscopy based on electronically controlled optical sampling," *Opt. Lett.* **35**, 3715–3717 (2010).
- M. Oeri, O. Peters, M. Wolfertetter, and R. Holzwarth, "Compact, high-speed sampling engine for pulsed femtosecond lasers," in *Terahertz Photonics* (SPIE, 2020), pp. 18–26.
- R. J. B. Dietz, N. Vieweg, T. Puppe, A. Zach, B. Globisch, T. Göbel, P. Leisching, and M. Schell, "All fiber-coupled THz-TDS system with kHz measurement rate based on electronically controlled optical sampling," *Opt. Lett.* **39**, 6482–6485 (2014).
- M. Yahyapour, A. Jahn, K. Dutzi, T. Puppe, P. Leisching, B. Schmauss, N. Vieweg, and A. Deninger, "Fastest thickness measurements with a terahertz time-domain system based on electronically controlled optical sampling," *Appl. Sci.* **9**, 1283 (2019).
- R. Kameyama, S. Takizawa, K. Hiramatsu, and K. Goda, "Dual-comb coherent Raman spectroscopy with near 100% duty cycle," *ACS Photonics* **8**, 975–981 (2021).
- F. Giorgetta, S. Potvin, J.-D. Deschênes, I. Coddington, N. Newbury, and E. Baumann, "Free-form dual-comb spectroscopy for compressive sensing and imaging," in review (2023).
- P. R. Griffiths and J. A. Haseth, *Fourier Transform Infrared Spectrometry* (Wiley-Interscience, 2007).
- P. Maslowski, K. F. Lee, A. C. Johansson, A. Khodabakhsh, G. Kowzan, L. Rutkowski, A. A. Mills, C. Mohr, J. Jiang, M. E. Fermann, and A. Foltynowicz, "Surpassing the path-limited resolution of Fourier-transform spectrometry with frequency combs," *Phys. Rev. A* **93**, 021802 (2016).
- A. Tourigny-Plante, P. Guay, and J. Genest, "Apodization in dual-comb spectroscopy for rapid measurement," in *Optical Sensors and Sensing Congress (2020)* (Optical Society of America, 2020), p. LTu3C.2.
- E. D. Caldwell, L. C. Sinclair, N. R. Newbury, and J.-D. Deschênes, "The time-programmable frequency comb and its use in quantum-limited ranging," *Nature* **610**, 667–673 (2022).
- N. R. Newbury, I. Coddington, and W. C. Swann, "Sensitivity of coherent dual-comb spectroscopy," *Opt. Express* **18**, 7929–7945 (2010).
- P. Martín-Mateos, F. U. Khan, and O. E. Bonilla-Manrique, "Direct hyperspectral dual-comb imaging," *Optica* **7**, 199–202 (2020).
- F. Ullah Khan, G. Guarnizo, and P. Martín-Mateos, "Direct hyperspectral dual-comb gas imaging in the mid-infrared," *Opt. Lett.* **45**, 5335–5338 (2020).
- F. U. Khan, A. Moreno-Oyervides, O. E. Bonilla-Manrique, and P. Martín-Mateos, "Sub-GHz optical resolution mid-infrared hyperspectral imaging with dual-comb," *Opt Lasers Eng.* **170**, 107799 (2023).
- T. Voumard, T. Wildi, V. Brasch, R. G. Álvarez, G. V. Ogando, and T. Herr, "AI-enabled real-time dual-comb molecular fingerprint imaging," *Opt. Lett.* **45**, 6583–6586 (2020).
- E. Vicentini, Z. Wang, K. Van Gasse, T. W. Hänsch, and N. Picqué, "Dual-comb hyperspectral digital holography," *Nat. Photonics* **15**, 890–894 (2021).
- S. W. Sharpe, T. J. Johnson, R. L. Sams, P. M. Chu, G. C. Rhoderick, and P. A. Johnson, "Gas-phase databases for quantitative infrared spectroscopy," *Appl. Spectrosc.* **58**, 1452–1461 (2004).
- L. S. Rothman, I. E. Gordon, A. Barbe, D. C. Benner, P. E. Bernath, M. Birk, V. Boudon, L. R. Brown, A. Campargue, J. P. Champion, K. Chance, L. H. Coudert, V. Dana, V. M. Devi, S. Fally, J. M. Flaud, R. R. Gamache, A. Goldman, D. Jacquemart, I. Kleiner, N. Lacombe, W. J. Lafferty, J. Y. Mandin, S. T. Massie, S. N. Mikhailenko, C. E. Miller, N. Moazzen-Ahmadi, O. V. Naumenko, A. V. Nikitin, J. Orphal, V. I. Perevalov, A. Perrin, A. Predoi-Cross, C. P. Rinsland, M. Rotger, M. Simeckova, M. A. H. Smith, K. Sung, S. A. Tashkun, J. Tennyson, R. A. Toth, A. C. Vandaele, and J. Vander Auwera, "The HITRAN 2008 molecular spectroscopic database," *J. Quant. Spectrosc. Radiat. Transfer* **110**, 533–572 (2009).
- D. Bannon, "Cubes and slices," *Nat. Photonics* **3**, 627–629 (2009).
- A. F. H. Goetz, G. Vane, J. E. Solomon, and B. N. Rock, "Imaging spectrometry for earth remote sensing," *Science* **228**, 1147–1153 (1985).
- X. Hadoux, F. Hui, J. K. H. Lim, C. L. Masters, A. Pébay, S. Chevalier, J. Ha, S. Loi, C. J. Fowler, C. Rowe, V. L. Villemagne, E. N. Taylor, C. Fluke, J.-P. Soucy, F. Lesage, J.-P. Sylvestre, P. Rosa-Neto, S. Mathotaarachchi, S. Gauthier, Z. S. Nasreddine, J. D. Arbour, M.-A. Rhéaume, S. Beaulieu, M. Dirani, C. T. O. Nguyen, B. V. Bui, R. Williamson, J. G. Crowston, and P. van Wijngaarden, "Non-invasive in vivo hyperspectral imaging of the retina for potential biomarker use in Alzheimer's disease," *Nat. Commun.* **10**, 4227 (2019).
- I. Amenabar, S. Poly, M. Goikoetxea, W. Nuansing, P. Lasch, and R. Hillenbrand, "Hyperspectral infrared nanoimaging of organic samples based on Fourier transform infrared nanospectroscopy," *Nat. Commun.* **8**, 14402 (2017).
- J. T. Friedlein, E. Baumann, K. A. Briggman, G. M. Colacion, F. R. Giorgetta, A. M. Goldfain, D. I. Herman, E. V. Hoenig, J. Hwang, N. R. Newbury, E. F. Perez, C. S. Yung, I. Coddington, and K. C. Cossel, "Dual-comb photoacoustic spectroscopy," *Nat. Commun.* **11**, 3152 (2020).
- T. Wildi, T. Voumard, V. Brasch, G. Yilmaz, and T. Herr, "Photo-acoustic dual-frequency comb spectroscopy," *Nat. Commun.* **11**, 4164 (2020).
- K. W. Young, B. P.-P. Kuo, S. M. O'Connor, S. Radic, and R. L. Lieber, "In Vivo sarcomere length measurement in whole muscles during passive stretch and twitch contractions," *Biophys. J.* **112**, 805–812 (2017).
- I. Coddington, W. C. Swann, and N. R. Newbury, "Coherent dual-comb spectroscopy at high signal-to-noise ratio," *Phys. Rev. A* **82**, 043817 (2010).